

Physics-Constrained Fine-Tuning of Flow-Matching Models for Generation and Inverse Problems

Jan Tauberschmidt¹, Sophie Fellenz², Sebastian J. Vollmer^{1,2}, Andrew B. Duncan³

¹ Department of Data Science and its Applications, German Research Centre for Artificial Intelligence (DFKI)

² Department of Computer Science, University of Kaiserslautern–Landau (RPTU)

³ Department of Mathematics, Imperial College London

Abstract

We present a framework for fine-tuning flow-matching generative models to enforce physical constraints and solve inverse problems in scientific systems. Starting from a model trained on low-fidelity or observational data, we apply a differentiable post-training procedure that minimizes weak-form residuals of governing partial differential equations (PDEs), promoting physical consistency and adherence to boundary conditions without distorting the underlying learned distribution. To infer unknown physical inputs, such as source terms, material parameters, or boundary data, we augment the generative process with a learnable latent parameter predictor and propose a joint optimization strategy. The resulting model produces physically valid field solutions alongside plausible estimates of hidden parameters, effectively addressing ill-posed inverse problems in a data-driven yet physics-aware manner. We validate our method on canonical PDE benchmarks, demonstrating improved satisfaction of PDE constraints and accurate recovery of latent coefficients. Our approach bridges generative modelling and scientific inference, opening new avenues for simulation-augmented discovery and data-efficient modelling of physical systems.

1 Introduction

Physical systems with rich spatio-temporal structure can be effectively represented by deep generative models, including diffusion and flow-matching methods (Kerrigan, Migliorini, and Smyth 2023; Erichson et al. 2025; Baldan et al. 2025; Price et al. 2024). Although their dynamics can be highly complex, these systems are often governed by fundamental principles, such as conservation laws, symmetries, and boundary conditions, that constrain the space of admissible solutions. Incorporating such physical structure into generative modelling can improve both sample fidelity and out-of-distribution generalization.

In many scientific domains, including atmospheric and oceanographic modelling, seismic inversion, and medical imaging, we often observe system states without access to the underlying physical parameters that govern them. Crucially, PDE-based constraints are typically parameter-dependent, with residuals that vary according to material properties, source terms, or other latent variables. Prior work has largely focused on simple or global constraints—such as fixed boundaries or symmetries, that apply uniformly across

the data distribution. Handling parameter-dependent constraints naively would require training over the joint distribution of solutions and parameters, which is often infeasible because parametric labels are missing, expensive to obtain, or high-dimensional.

Addressing this limitation is critical for scientific discovery. Many inverse problems in the natural sciences and engineering require reasoning about unobserved parameters or exploring hypothetical scenarios inaccessible to direct experimentation. A generative model that can enforce parameter-dependent PDE constraints using only observational data would provide a powerful tool for data-efficient simulation, hypothesis testing, and the discovery of new physical phenomena, helping to bridge the gap between raw observations and mechanistic understanding.

This work proposes a framework for fine-tuning flow-matching generative models to enforce parameter-dependent PDE constraints without requiring joint parameter–solution training data. This work aligns with a growing trend of simulation-augmented machine learning (Karniadakis et al. 2021), where generative models accelerate scientific discovery by efficiently exploring physically plausible solution spaces. Our approach reformulates fine-tuning as a stochastic optimal control problem via Adjoint Matching (Domingo-Enrich et al. 2025), guided by weak-form PDE residuals. By augmenting the model with a latent parameter evolution, we enable joint generation of physically consistent solution–parameter pairs, addressing ill-posed inverse problems.

We evaluate our proposed fine-tuning framework on two canonical physical systems. We demonstrate denoising and conditional generation capabilities, including robustness to noisy data and the ability to infer latent parameters from sparse observations. Visual and quantitative results, including strong reductions in residuals across tasks and robustness to model misspecification, highlight the flexibility of our method for integrating physical constraints into generative modelling.

To sum up, our contributions are as follows:

- **POST-TRAINING ENFORCEMENT OF PHYSICAL CONSTRAINTS:** We introduce a fine-tuning strategy that tilts the generative distribution toward PDE-consistent samples using weak-form residuals, improving physical validity while preserving diversity.

- **ADJOINT-MATCHING FINE-TUNING WITH THEORETICAL GROUNDING:** Leveraging the adjoint-matching framework, we recast reward-based fine-tuning as a stochastic control problem, extending flow-matching models to generate latent parameters alongside states, enabling inverse problem inference without paired training data.
- **BRIDGING GENERATIVE MODELING AND PHYSICS-INFORMED LEARNING:** Our approach connects preference-aligned generation with physics-based inference, enabling simulation-augmented models to generate solutions that respect complex physical laws.

2 Related Work

Physics-Constrained Generative Models Integrating physical constraints—such as boundary conditions, symmetry invariances, and partial differential equation (PDE) constraints—into machine learning models improves both accuracy and out-of-distribution generalization. Classical approaches, such as Physics-Informed Neural Networks (PINNs) (Raissi, Perdikaris, and Karniadakis 2019), directly regress solutions that satisfy governing equations. While effective for forward or inverse problems, PINNs do not capture distributions over solutions, making them unsuitable for generative tasks that require sampling diverse plausible outcomes.

In the generative setting, the main challenge is ensuring that the physically constrained samples retain the variability of the underlying generative model, avoiding pathological issues such as mode collapse. Bastek, Sun, and Kochmann (2024) proposes a unified framework for introducing physical constraints into Denoising Diffusion Probabilistic Models (DDPMs) (Ho, Jain, and Abbeel 2020) at pre-training time, by adding a first-principles physics-residual loss to the diffusion training objective. This loss penalises violations of governing PDEs (e.g. fluid dynamics equations) so that generated samples inherently satisfy physical laws. The method was empirically shown to reduce residual errors for individual samples significantly, while simultaneously acting as a regulariser against overfitting, thereby improving generalisation. To evaluate the physics-residual loss, one needs to compute the expected PDE residual of the final denoised sample conditioned on the current noisy state in the DDPM process. Accurately estimating this expectation requires generating multiple reverse-diffusion trajectories from the same noisy sample, which makes pre-training significantly more expensive. A common alternative is to use Tweedie’s formula to approximate the conditional expectation in a single pass, but this shortcut introduces bias, particularly in the final denoising steps.

Zhang and Zou (2025) proposes enforcing constraints through a post-hoc distillation stage, where a deterministic student model is trained from a vanilla diffusion model to generate samples in one-step, regularised by a PDE residual loss. In (Wang et al. 2025) the authors introduce PhyDA, diffusion-based data assimilation framework that ensures reconstructions obey PDE-based dynamics, specifically for atmospheric science. An autoencoder is used to encode sparse

observations into a structured latent prior for the diffusion model, which is trained with an additional physical residual loss.

Inference- and Post-Training Constraint Enforcement

Various works have proposed approaches to enforce PDE constraints at inference time, often in combination with observational constraints, drawing connections to conditional diffusion models (Dhariwal and Nichol 2021; Ho and Salimans 2021). Huang et al. (2024) introduce guidance terms within the denoising update of a score-based diffusion model to steer the denoising process towards solutions which are both consistent with data and underlying PDEs. A related approach was considered by Xu et al. (2025), further introducing an adaptive constraint to mitigate instabilities in early diffusion steps. In (Christopher, Baek, and Fioretto 2024), the authors recast the inference-time sampling of a diffusion process as a constrained optimization problem, each diffusion step is projected to satisfy user-defined constraints or physical principles. This allows strict enforcement of hard constraints (including convex and non-convex constraints, as well as ODE-based physical laws) on the generated data. Lu and Xu (2024) consider the setting where the base diffusion model is trained on cheap, low-fidelity simulations, leveraging a similar approach to generate down-scaled samples via projection.

Flow-Matching Models for Simulation and Inverse Problems

Flow-matching (FM) (Lipman et al. 2023) has emerged as a flexible generative modelling paradigm for complex physical systems across science, including molecular systems (Hassan et al. 2024), weather (Price et al. 2024) and geology (Zhang, Li, and Huang 2024). In the context of physics-constrained generative models (Utkarsh et al. 2025) introduces a zero-shot inference framework to enforce hard physical constraints in pretrained flow models, by repeatedly projecting the generative flow at sampling time. Similarly, (Cheng et al. 2024) proposed the ECI algorithm, to adapt a pretrained flow-matching model so that it exactly satisfies constraints without using analytical gradients. In each iteration of flow sampling, ECI performs: an Extrapolation step (advancing along the learned flow), a Correction step (applying a constraint-enforcement operation), and an Interpolation step (adjusting back towards the model’s trajectory). While projection approaches are a compelling strategy for hard constraints, they can be challenging particularly for local constraints such as boundary conditions, as direct enforcement can introduce discontinuities. The above approach mitigates this by interleaving projections with flow steps, however this relies on the flow’s ability to rapidly correct such non-physical artifacts.

Baldan et al. (2025) propose Physics-Based Flow Matching (PBFM), which embeds constraints (PDE or symmetries) directly into the FM loss during training. The approach leverages temporal unrolling to refine noise-free final state predictions and jointly minimizes generative and physics-based losses without manual hyperparameter tuning of their tradeoff. To mitigate conflicts between physical constraints and the data loss, they employ the CONFIG (Liu, Chu, and Thuerey 2024), which combines the gradients of both losses

in a way that ensures that gradient updates always minimise both losses simultaneously.

Related to our approach are the works on generative models for Bayesian inverse problems (Stuart 2010), where the goal is to infer distributions over latent PDE parameters given partial or noisy observations. Conditional diffusion and flow-matching models can be used to generate samples from conditional distributions and posterior distributions, supporting amortized inference and uncertainty quantification (Song et al. 2021; Utkarsh et al. 2025; Zhang, Rao, and Agrawala 2023). Conditioning is typically achieved either through explicit parameter inputs or guidance mechanisms during sampling, as in classifier-guided diffusion. While effective when large volumes of paired training data is available, these approaches are less relevant to observational settings where parameters are unobserved. In contrast, our approach connects the observed data to the latent parameters only during post-training, requiring substantially smaller volumes of data.

3 Method

FM models are trained to learn and sample from a given distribution of data p_{data} . They approximate this distribution by constructing a Markovian transformation from noise to data, such that the time marginals of this transformation match those of a *reference flow* $X_t = \beta_t X_1 + \gamma_t X_0$. Specifically FM models learn a vector field $v_t(x)$ that transports noise to data, via the ODE $dX_t = v_t(X_t)$. We can optionally inject a noise schedule $\sigma(t)$ along the trajectory to define an equivalent SDE that preserves the same time marginals (Maoutsa, Reich, and Opper 2020),

$$\begin{aligned} dX_t &= \left(v_t(X_t) + \frac{\sigma(t)^2}{2\eta_t} \left(v_t(X_t) - \frac{\dot{\beta}_t}{\beta_t} X_t \right) \right) + \sigma(t) dB_t \\ &=: b_t(X_t) + \sigma(t) dB_t, \end{aligned}$$

where $\eta_t = \gamma_t \left(\frac{\dot{\beta}_t}{\beta_t} \gamma_t - \dot{\gamma}_t \right)$.

Assuming we have access to a FM model which generates samples according to distribution $p(x)$, we seek to adjust this model so as to generate samples from the tilted distribution $p_r(x) \propto e^{\lambda r(x)} p(x)$, where r is a reward function and λ characterises the degree of distribution shift induced by fine-tuning.

To achieve this, we leverage the adjoint-matching framework of (Domingo-Enrich et al. 2025). This work reformulates reward fine-tuning for flow-based generative models as a control problem in which the base generative process given by v_t^{base} is steered toward high-reward samples via modifying the learned vector field, which we denote as v_t^{ft} with corresponding drift term b_t^{ft} . Our approach is conceptually related to reward- or preference-based fine-tuning of generative models (Christiano et al. 2017; Sun et al. 2024), where a learned or computed reward steers generation toward desired properties. Here, the reward is defined via PDE residuals, encoding knowledge about underlying dynamics and physical constraints to the solutions space as deviations to differential operators or boundary conditions.

Notably, we assume that the distribution generated by the base model $p(x)$ only captures an observed quantity, but does not provide us with corresponding parameters or coefficient fields often needed to evaluate the respective differential operator. In the following, we will present a strategy of jointly recovering unknown parameters and fine-tuning the generation process.

Reward

A generative model can reproduce the visual characteristics of empirical data while ignoring the physics that governs it, thereby rendering the samples unusable for downstream scientific tasks. To bridge this gap we impose the known governing equations as *soft constraints*, expressed through differential operators $\mathcal{L}_\alpha x = 0$ with parameters α . Throughout, a generated sample x is interpreted as the discretisation of a continuous field $x(\xi)$ on a domain Ω . Boundary information is captured either by Dirichlet conditions $x(\xi) = h(\xi)$ or Neumann conditions $\partial_n x(\xi) = \tilde{h}(\xi)$ for $\xi \in \partial\Omega$.

The *strong* PDE residual is defined as

$$\mathcal{R}_{\text{strong}}(x, \alpha) = \|\mathcal{L}_\alpha x\|_{L^2(\Omega)}^2,$$

and deviations from the boundary data are measured by \mathcal{R}_{BC} . In practice, strong residuals involve high-order derivatives that make the optimization landscape unstable. We therefore adopt *weak-form residuals*, which only require first-order derivatives and remain numerically stable under noisy or misspecified data, of the form $\langle \mathcal{L}_\alpha x, \psi \rangle_{L^2(\Omega)}$ for suitably chosen test functions $\psi \in \Psi$. Repeated applications of integration-by-parts will transfer derivatives from x to ψ until only first-order derivatives of x remain, which is sufficient for the problems considered.

The set Ψ is composed of radially symmetric, compactly supported local polynomial kernels. For each evaluation we draw N_{test} such functions; their centers and length-scales are sampled at random. A mollifier enforces $\psi|_{\partial\Omega} = 0$, justifying the integration by parts. The resulting residual is

$$\mathcal{R}_{\text{weak}}(x, \alpha) = \frac{1}{N_{\text{test}}} \sum_{i=1}^{N_{\text{test}}} |\langle \mathcal{L}_\alpha x, \psi^{(i)} \rangle_{L^2(\Omega)}|^2.$$

These randomly sampled local test functions act as stochastic probes of PDE violations, providing a low-variance, data-efficient learning signal. A more detailed description of the test functions used can be found in Appendix C.

Joint Evolution

Fine-tuning is nontrivial in our setting because we must infer latent physical parameters jointly with the generated solutions. On fully denoised samples, we can train an inverse predictor, i.e., $\varphi(x_1) = \alpha_1$, such that the weak PDE residual is minimised. As a naïve approach, this already induces a joint distribution over (x_1, α_1) via the push-forward through φ .

However, we advocate a more principled formulation that evolves *both* x and α along vector fields, enabling joint sampling of parameters and solutions, as well as a controlled regularisation of fine-tuning through the Adjoint Matching framework as outlined below. In the fine-tuning model,

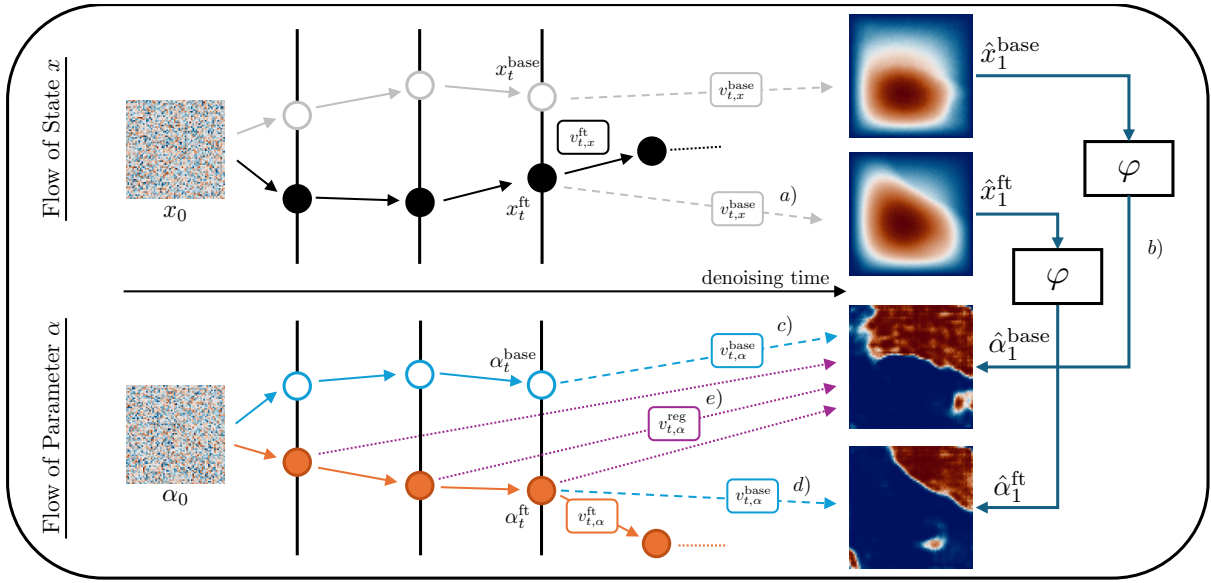


Figure 1: Visual depiction of proposed method. Starting at state x_t^{base} or x_t^{ft} , we use the base vector field $v_{t,x}^{\text{base}}$ to predict the final sample [a)]. Through the inverse predictor φ , we recover the corresponding predicted parameters $\hat{\alpha}_1^{\text{base}}$ and $\hat{\alpha}_1^{\text{ft}}$ [b)]. These estimates can be used as a target for evolving α_t^{base} [c)] or as a baseline for the fine-tuned evolution of α_t^{ft} [d)]. For purposes of regularization, we further consider $v_{t,\alpha}^{\text{reg}}$, pointing from the current α_t^{ft} to the predicted final parameter of the base evolution $\hat{\alpha}_1^{\text{base}}$ [e)].

this can be achieved by directly learning the vector field $v_{t,\alpha}^{\text{ft}}$ jointly with $v_{t,x}^{\text{ft}}$ by augmenting the neural architecture. Since no ground-truth flow of α for the base model is available, at each state (x_t, α_t) we define a *surrogate base flow* using the inverse predictor φ . Specifically, we consider the one-step estimates

$$\hat{x}_1 = x_t + (1-t)v_t^{\text{base}}(x_t), \quad \hat{\alpha}_1 = \varphi(\hat{x}_1)$$

The direction from the current state α_t to the predicted final parameter $\hat{\alpha}_1$ serves as a base vector field which we use to evolve alpha, i.e. $v_{t,\alpha}^{\text{base}}(\alpha_t) = (\hat{\alpha}_1 - \alpha_t)/(1-t)$ inducing corresponding drift $b_{t,\alpha}^{\text{base}}$. This *surrogate base flow*, starting at a noise sample $\alpha_0^{\text{base}} \sim \mathcal{N}(0, I)$, emulates a denoising process of the recovered parameter. We denote by α^{base} the parameter aligned with the base trajectory x^{base} . While the evolution of α^{base} does not influence the trajectory of x^{base} , the inferred vector field can be used to effectively regularize the generation of the fine-tuned model.

Similarly, to regularise towards the parameter recovered under the base model, we introduce an additional field $v_{t,\alpha}^{\text{reg}}(\alpha_t^{\text{ft}}) = (\hat{\alpha}_1^{\text{base}} - \alpha_t^{\text{ft}})/(1-t)$. This vector field points from the current parameter estimate of the fine-tuned trajectory α_t^{ft} to the recovered parameter under the base model $\hat{\alpha}_1^{\text{base}}$. The field is used to pull the fine-tuned dynamics towards final samples associated with parameters similar to those of the base trajectory. The introduced vector fields are visualized in Fig. 1.

Adjoint Matching

Considering an augmented state variable of the joint evolution $\tilde{X}_t = (X_t^T, \alpha_t^T)^T$, we cast fine-tuning as a stochastic

optimal control problem:

$$\begin{aligned} \min_{\tilde{u}} \mathbb{E} \left[\int_0^1 \left(\frac{1}{2} \|\tilde{u}_t(\tilde{X}_t)\|^2 + f(\tilde{X}_t) \right) dt + g(\tilde{X}_1) \right] \\ \text{s.t. } d\tilde{X}_t = \left(\tilde{b}_t^{\text{base}}(\tilde{X}_t) + \sigma(t) \tilde{u}_t(\tilde{X}_t) \right) dt + \sigma(t) d\tilde{B}_t \end{aligned} \quad (1)$$

with control $\tilde{u}_t(\tilde{X}_t)$, running state cost $f(\tilde{X}_t)$, and terminal cost $g(\tilde{X}_1)$. In this formulation, fine-tuning amounts to a point-wise modification of the base drift through application of control \tilde{u} , i.e.

$$\tilde{b}_t^{\text{ft}}(\tilde{X}_t) = \tilde{b}_t^{\text{base}}(\tilde{X}_t) + \sigma(t) \tilde{u}_t(\tilde{X}_t).$$

In (Domingo-Enrich et al. 2025), Adjoint Matching is introduced as a technique with lower variance and computational cost than standard adjoint methods. The method is based on a *Lean Adjoint* state, which is initialized as

$$\tilde{a}_1^T = \tilde{\lambda} \nabla_{\tilde{x}} g(\tilde{X}_1) = (\lambda_x \nabla_x g(X_1, \alpha_1), \lambda_\alpha \nabla_\alpha g(X_1, \alpha_1))$$

and evolves backward in time according to

$$\begin{aligned} \frac{d}{dt} \tilde{a}_t &= - \left(\nabla_{\tilde{x}} \tilde{b}_t^{\text{base}}(\tilde{X}_t)^T \tilde{a}_t + \nabla_{\tilde{x}} f(\tilde{X}_t)^T \right) \\ &= - \begin{pmatrix} J_{xx}^T & J_{\alpha x}^T \\ J_{x\alpha}^T & J_{\alpha\alpha}^T \end{pmatrix} \begin{pmatrix} a_{t,x} \\ a_{t,\alpha} \end{pmatrix} - \begin{pmatrix} \nabla_x f(X_t, \alpha_t)^T \\ \nabla_\alpha f(X_t, \alpha_t)^T \end{pmatrix} \end{aligned} \quad (2)$$

where the block-Jacobian is evaluated along the base drift for X and α , which means that $J_{ij} = \nabla_j b_{t,i}^{\text{base}}(X_t, \alpha_t)$ for $i, j \in \{x, \alpha\}$. The hyperparameters λ_x and λ_α can be used to regulate the extent to which the fine-tuned distribution departs from the base distribution.

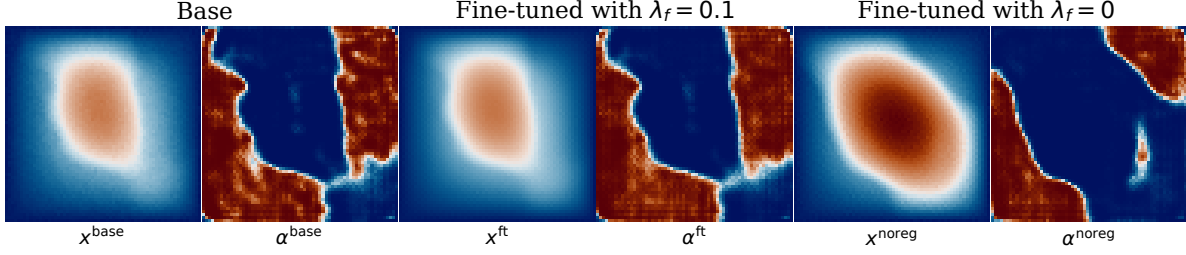


Figure 2: Denoising results for the Darcy test case for the same noise samples. Left: noisy input pressure field and its inferred permeability. Middle: fine-tuned output with parameter regularisation ($\lambda_f = 0.1$). Right: fine-tuning without regularisation. With regularisation the fine-tuned solution effectively suppresses noise while preserving the permeability-induced structural details captured by the base model. (Color maps throughout this work taken from (Crameri, Shephard, and Heron 2020))

The *Adjoint Matching* objective can then be formulated as a consistency loss:

$$\begin{aligned} \mathcal{L}(\tilde{u}; \tilde{X}) &= \frac{1}{2} \int_0^1 \|\tilde{u}_t(\tilde{X}_t) + \sigma(t) \tilde{a}_t\|^2 dt \\ &= \frac{1}{2} \int_0^1 \left(\|u_{t,x}(X_t, \alpha_t) + \sigma(t) a_{t,x}\|^2 \right. \\ &\quad \left. + \|u_{t,\alpha}(X_t, \alpha_t) + \sigma(t) a_{t,\alpha}\|^2 \right) dt. \end{aligned} \quad (3)$$

It can be shown (see (Domingo-Enrich et al. 2025)) that with $f = 0$, this objective is consistent with the tilted target distribution for reward $r = -g$, if optimized with a *memoryless* noise schedule. This noise schedule is defined as $\sigma(t) = \sqrt{2\eta_t}$. It ensures sufficient mixing during generation such that the final sample X_1 is independent of X_0 .

Equation 1 is optimized by iteratively sampling trajectories with the fine-tuned model while following a memoryless noise schedule, numerically computing the lean adjoint states by solving the ODE in Equation 2, and taking a gradient descent step to minimize the loss in Equation 3. Note that gradients are only computed through the control \tilde{u}_t and not through the adjoint, reducing the optimization target to a simple regression loss. We state the full training algorithm and implementation details in Appendix C.

Adjoint Matching steers the generator toward the reward-tilted distribution, thereby reshaping the entire output distribution rather than correcting individual trajectories. However, when fine-tuning observational data or under system misspecification, we might be interested in retaining sample-specific detail. Empirically we find that this can be effectively encoded by imposing similarity of the inferred coefficients between base and fine-tuned model. Therefore, we add a running state cost

$$f(\alpha) = \lambda_f \left\| v_{t,\alpha}^{\text{ft}}(\alpha) - v_{t,\alpha}^{\text{reg}}(\alpha) \right\|^2$$

which penalises deviations of the fine-tuned α -drift from the direction pointing toward the base estimate $\hat{\alpha}_1^{\text{base}}$. The hyper-parameter λ_f controls a smooth trade-off: $\lambda_f = 0$

recovers pure Adjoint Matching, while larger λ_f progressively anchors the final parameters α_1 obtained under the fine-tuned model to their base-model counterparts, thus retaining trajectory-level detail.

4 Experiments

We demonstrate our method on two PDE systems and cover a broad spectrum of inverse-problem tasks. The experiments span denoising of observational data, guidance from sparse measurements after fine-tuning, super-resolution, and the enforcement of reflective and misspecified boundary conditions. Hyperparameters and training specifics are given in Appendix D.

Darcy Flow: We consider a square domain of $\Omega = [0, 1]^2$ where a permeability $a(\xi)$ and a forcing term $f(\xi)$ induce a pressure distribution $x(\xi)$. We observe solutions for samples of permeability $a \sim \mu_a$, drawn from a discretized Gaussian Process such that a takes values $a \in \{3, 12\}$. Pressure x follows the law

$$-\nabla \cdot (a(\xi) \nabla x(\xi)) - f(\xi) = 0, \quad x \in \Omega.$$

We usually assume zero Dirichlet boundary conditions. This is a standard dataset used in the Neural Operator literature, established in (Li et al. 2021).

Acoustics: Here we consider an acoustic wave equation on $\Omega = [0, 1]^2$ observed for $t \in [0, T]$ with sampled speed of sound $c(\xi)$, representing changing material properties. Again, we sample $c \sim \mu_c$ from a discretized 2D Gaussian process with values $c \in \{2, 3\}$, which leads to complex acoustic scattering. Boundaries are assumed to be reflective. Starting from an initial condition composed of four isotropic Gaussians equally spaced along both axes, the evolution of pressure is described by:

$$\partial_t^2 x(t, \xi) - c(\xi)^2 \Delta x(t, \xi) = 0, \quad (\xi, t) \in \Omega \times [0, T].$$

More detail about the data and its generation is given in Appendix A. For all experiments, we train a FM model on the generated data. As the backbone of the base model we choose a U-FNO (Wen et al. 2022) architecture due to its ability to model sharp edges and local phenomena. Then, before fine-tuning, we pre-train the inverse predictor φ , mapping final samples x_1 to parameters α_1 to minimize the weak

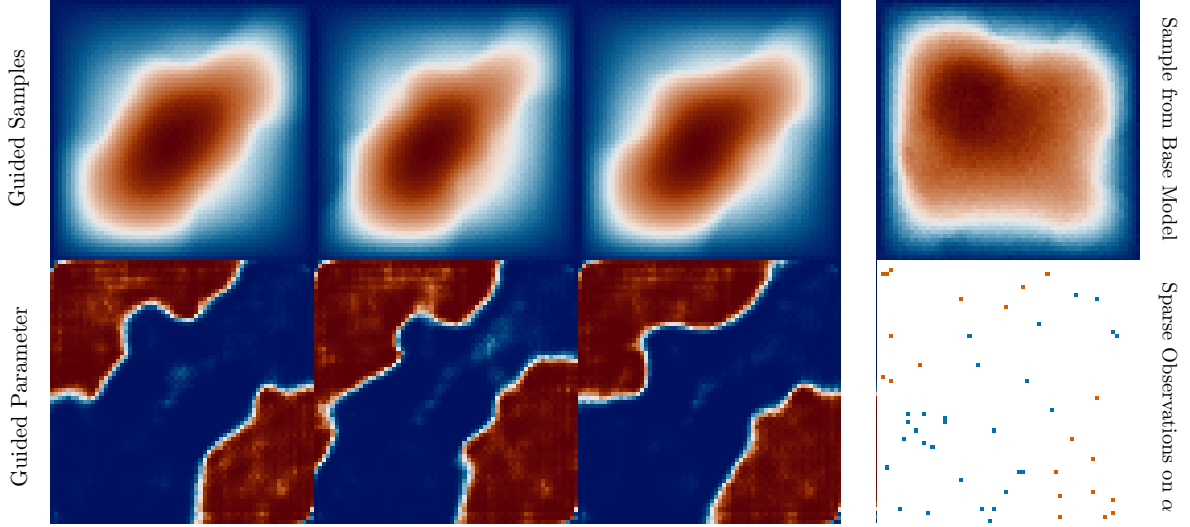


Figure 3: Parameter-space guidance from sparse observations. The columns on the left show three independent pressure-permeability samples obtained with guidance toward sparse observations on the right. Although the base model was pre-trained solely on observational pressure data, fine-tuning recovers the joint distribution and enables generation of high-quality samples that adhere to the measurements while retaining realistic variability.

residual loss $\mathcal{R}_{\text{weak}}$ on a fixed number of samples generated from the base FM model. As in (Domingo-Enrich et al. 2025), we initialize the fine-tuning model with the same weights as the base model. However, to inform $v_{t,x}^{\text{ft}}$ about the current parameter α_t , we add conditioning layers to the architecture. Additionally, a separate output head for $v_{t,\alpha}$ is added to the model. During fine-tuning, samples are generated using the memoryless noise schedule. Reported results however are all generated without injected noise, i.e. $\sigma(t) = 0$. Details about the implementation can be found in Appendix C.

Observational Data

When working with real-world measured data, we typically face observational noise. In this example, we pre-train a FM model on a noisy version of the Darcy flow dataset, meaning that we add i.i.d noise to each spatial location $\tilde{x}(\xi_i) = x(\xi_i) + \sigma \varepsilon_i$ with $\varepsilon_i \sim \mathcal{N}(0, I)$. During fine-tuning, we minimize the weak PDE residual. This denoising experiment highlights the role of parameter-space regularisation. With a moderate regularisation weight $\lambda_f = 0.1$ the optimiser suppresses the noise yet stays close to the base permeability, as seen in Fig. 2.

Table 1 compares weak and strong PDE residuals for base FM models trained clean and noisy data respectively, and the corresponding fine-tuned model on the noisy data. For the FM models permeability fields are obtained from the pre-trained inverse predictor φ . Fine-tuning reduces both residuals substantially demonstrating the efficacy of weak-form optimisation in the presence of noise.

To ensure that denoising does not collapse the generative spread we compare mean- and variance-matching scores as

Table 1: Weak- and strong-form PDE residuals for the Darcy denoising experiment averaged over 128 samples. Residuals of the data are given for reference.

Model	$\mathcal{R}_{\text{weak}}$	$\mathcal{R}_{\text{strong}}$
Base FM	$(4.6 \pm 2.0) \times 10^{-1}$	$(8.3 \pm 4.2) \times 10^{-1}$
Noisy FM	$(9.3 \pm 1.5) \times 10^{-1}$	$(1.8 \pm 0.2) \times 10^1$
Fine-tuned	$(2.4 \pm 0.6) \times 10^{-1}$	5.6 ± 0.9
Noisy data	$(9.6 \pm 0.7) \times 10^{-1}$	$(2.7 \pm 0.3) \times 10^1$
Data	$(1.0 \pm 0.3) \times 10^{-1}$	1.4 ± 1.0

well as sample diversity between the base and fine-tuned models (metrics follow (Kerrigan, Migliorini, and Smyth 2023) and are normalised by the data variance, details in Appendix D). With $\lambda_f = 0.1$ these statistics remain similar to the base model, indicating that the overall distribution is preserved. Without regularisation, diversity in the permeability field drops sharply and the pressure distribution drifts accordingly. Since this result depends on other hyperparameters, such as λ_x , we provide further illustrative results in Appendix E

Guidance and Conditional Generation

In many realistic settings dense observations of a state variable are available for pre-training a generative model, whereas only a few measurements of the latent parameter can be collected. To sample from the posterior of parameter-state pairs that respect such sparse evidence we steer the generative process through *guidance*. Guiding sampling on learned quantities is a common practise for tasks like im-

Table 2: Pointwise statistics indicating sample quality and diversity following (Kerrigan, Migliorini, and Smyth 2023). Based on 256 samples.

Metric	Base FM	FT	FT ($\lambda_f = 0$)
MMSE _{rel} x	1.02×10^{-2}	1.20×10^{-2}	2.42
SMSE _{rel} x	1.06×10^{-3}	1.01×10^{-3}	2.71×10^{-2}
MMSE _{rel} α	2.53×10^{-2}	2.35×10^{-2}	3.97×10^{-1}
SMSE _{rel} α	3.13×10^{-2}	3.27×10^{-2}	1.95×10^{-1}
Diversity _{rel} x	9.85×10^{-1}	9.88×10^{-1}	1.21
Diversity _{rel} α	7.01×10^{-1}	6.97×10^{-1}	4.29×10^{-1}

age inpainting, see (Bansal et al. 2023; Song et al. 2021). For physical data, (Huang et al. 2024) demonstrates guided sampling towards sparse observations from a model that was pre-trained on the joint parameter-state distribution. Our approach applies the same guidance mechanism, however, to a model that was pre-trained on state observations alone.

Let $\alpha^* = \{(\xi_i, \alpha_i^*)\}_{i=1}^m$ denote the observed parameter values and locations. The normalised mean-squared discrepancy

$$\mathcal{L}_{\text{guide}} = \frac{1}{m} \sum_{i=1}^m |\hat{\alpha}_1^{\text{ft}}(\xi_i) - \alpha_i^*|^2$$

provides a steering signal, which we inject into each Euler step as

$$\tilde{x}_{t+\Delta t} = \tilde{x}_t + \Delta t \tilde{v}_t^{\text{ft}}(\tilde{x}_t) - \zeta \Delta t \nabla_{\tilde{x}} \mathcal{L}_{\text{guide}}$$

with $\zeta > 0$ controlling the conditioning strength. Figure 3 confirms that the guided sampler adheres to the sparse measurements while preserving realistic variability. Additional examples are given in Appendix E.

Super-Resolution and Reflective Boundary in 3D

Spatio-temporal acoustic wave propagation is numerically demanding: sharp material discontinuities combined with reflective boundaries produce intricate scattering patterns that are costly to resolve. We represent every space-time pressure field as a three-dimensional sample $x \in \mathbb{R}^{64 \times 64 \times 64}$ obtained from a low-fidelity solver and train a base Flow-Matching model on this data. At test time the model outputs of pressure and the recovered parameter field c are up-sampled by a factor of four through trilinear interpolation and weak PDE residuals and reflective-boundary penalties are evaluated on the 256^3 grid. Because naïve interpolation fails to enforce the zero-normal-gradient boundary condition, fine-tuning is essential. Table 3 shows that fine-tuning is able to significantly reduce the residual of the reflective boundary \mathcal{R}_{BC} , defined as the mean of the squared magnitude of the normal gradient at the boundary, while still adhering to the physical laws imposed by the PDE, indicated by slightly lower weak residuals. We visually present results in Appendix E.

Misspecification

We finally assess the robustness of our fine-tuning procedure to *misspecified* training data. Starting from the 2-D stationary Darcy setup, we prescribe a non-zero Dirichlet condition on the top $x(\xi_1, 1) = \sin(\pi \xi_1)$, while keeping zero

Table 3: Acoustic-wave test case: weak residual $\mathcal{R}_{\text{weak}}$ and reflective-boundary residual \mathcal{R}_{BC} across 20 generated samples. Fine-tuning sharply reduces the boundary error while further lowering the weak residual.

Model	$\mathcal{R}_{\text{weak}}$	\mathcal{R}_{BC}
Base	$(4.0 \pm 0.8) \times 10^{-3}$	$(2.6 \pm 0.1) \times 10^{-1}$
Fine-tuned	$(2.2 \pm 0.6) \times 10^{-3}$	$(8.0 \pm 0.4) \times 10^{-2}$

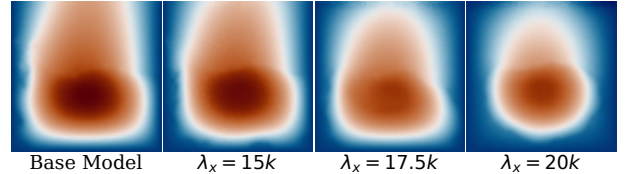


Figure 4: Misspecified-boundary experiment. Each column shows a pressure field generated from the same initial noise but from models fine-tuned with increasing λ_x .

boundary values elsewhere. During fine-tuning, however, we deliberately enforce homogeneous Dirichlet data together with the weak PDE residual. Fig. 4 shows fine-tuning results for different strengths of λ_x for the same noise sample. As λ_x increases, the samples conform progressively better to the desired zero boundary without sacrificing physical plausibility, even though the model must extrapolate far beyond its pre-training domain. Owing to parameter regularisation $\lambda_f > 0$, the fine-tuned solutions still preserve sample-specific permeability features. Additional visualisations, for example with $\lambda_f = 0$, and a comparison with ECI (Cheng et al. 2024) are provided in Appendix E.

5 Conclusion

We have introduced a framework for post-training fine-tuning of flow-matching generative models to enforce physical constraints and jointly infer latent physical parameters informing the constraints. Through a novel architecture, combined with the combination of weak-form PDE residuals with an adjoint-matching scheme our method can produce samples that adhere to complex constraints without significantly affecting the sample diversity. Preliminary experiments on Darcy flow and acoustic wave problems demonstrate the potential of this method to reduce residuals and enable joint solution-parameter generation, supporting its promise for physics-aware generative modelling.

Future steps include adaptive approaches to optimising trade-off between constraint enforcement and generative diversity, and extending the framework to more complex and multi-physics systems, including coupled PDEs and stochastic or chaotic dynamics. We would also explore how this methodology can be leveraged for uncertainty quantification and propagation, and downstream tasks such as optimal sensor placement and scientific discovery workflows.

Acknowledgments

This work was supported by funding from the German Federal Ministry for Education and Research (Bundesministerium für Bildung und Forschung, BMBF) within the project 'Physics Informed Anomaly Detection' (grant number 01IS24071).

References

- Baldan, G.; Liu, Q.; Guardone, A.; and Thuerey, N. 2025. Flow Matching Meets PDEs: A Unified Framework for Physics-Constrained Generation. *arXiv preprint arXiv:2506.08604*.
- Bansal, A.; Chu, H.-M.; Schwarzschild, A.; Sengupta, S.; Goldblum, M.; Geiping, J.; and Goldstein, T. 2023. Universal Guidance for Diffusion Models. *arXiv:2302.07121*.
- Bastek, J.-H.; Sun, W.; and Kochmann, D. 2024. Physics-Informed Diffusion Models. In *The Thirteenth International Conference on Learning Representations*.
- Cheng, C.; Han, B.; Maddix, D. C.; Ansari, A. F.; Stuart, A.; Mahoney, M. W.; and Wang, Y. 2024. Gradient-free generation for hard-constrained systems. *arXiv preprint arXiv:2412.01786*.
- Christiano, P. F.; Leike, J.; Brown, T.; Martic, M.; Legg, S.; and Amodei, D. 2017. Deep reinforcement learning from human preferences. *Advances in neural information processing systems*, 30.
- Christopher, J. K.; Baek, S.; and Fioretto, N. 2024. Constrained synthesis with projected diffusion models. *Advances in Neural Information Processing Systems*, 37: 89307–89333.
- Crameri, F.; Shephard, G.; and Heron, P. 2020. The misuse of colour in science communication. *Nature Communications*, 11.
- Dhariwal, P.; and Nichol, A. 2021. Diffusion models beat gans on image synthesis. *Advances in neural information processing systems*, 34: 8780–8794.
- Domingo-Enrich, C.; Drozdal, M.; Karrer, B.; and Chen, R. T. Q. 2025. Adjoint Matching: Fine-tuning Flow and Diffusion Generative Models with Memoryless Stochastic Optimal Control. *arXiv:2409.08861*.
- Erichson, N. B.; Mikuni, V.; Lyu, D.; Gao, Y.; Azencot, O.; Lim, S. H.; and Mahoney, M. W. 2025. FLEX: A Backbone for Diffusion-Based Modeling of Spatio-temporal Physical Systems. *arXiv:2505.17351*.
- Hassan, M.; Shenoy, N.; Lee, J.; Stark, H.; Thaler, S.; and Beaini, D. 2024. ET-Flow: Equivariant Flow-Matching for Molecular Conformer Generation. *arXiv:2410.22388*.
- Ho, J.; Jain, A.; and Abbeel, P. 2020. Denoising diffusion probabilistic models. *Advances in neural information processing systems*, 33: 6840–6851.
- Ho, J.; and Salimans, T. 2021. Classifier-Free Diffusion Guidance. In *NeurIPS 2021 Workshop on Deep Generative Models and Downstream Applications*.
- Huang, J.; Yang, G.; Wang, Z.; and Park, J. J. 2024. DiffusionPDE: Generative PDE-Solving Under Partial Observation. *arXiv:2406.17763*.
- Karniadakis, G. E.; Kevrekidis, I. G.; Lu, L.; Perdikaris, P.; Wang, S.; and Yang, L. 2021. Physics-informed machine learning. *Nature Reviews Physics*, 3(6): 422–440.
- Kerrigan, G.; Migliorini, G.; and Smyth, P. 2023. Functional Flow Matching. *arXiv:2305.17209*.
- Li, Z.; Kovachki, N.; Azizzadenesheli, K.; Liu, B.; Bhattacharya, K.; Stuart, A.; and Anandkumar, A. 2021. Fourier Neural Operator for Parametric Partial Differential Equations. *arXiv:2010.08895*.
- Lipman, Y.; Chen, R. T. Q.; Ben-Hamu, H.; Nickel, M.; and Le, M. 2023. Flow Matching for Generative Modeling. *arXiv:2210.02747*.
- Liu, Q.; Chu, M.; and Thuerey, N. 2024. Config: Towards conflict-free training of physics informed neural networks. *arXiv preprint arXiv:2408.11104*.
- Lu, Y.; and Xu, W. 2024. Generative downscaling of PDE solvers with physics-guided diffusion models. *Journal of scientific computing*, 101(3): 71.
- Maoutsa, D.; Reich, S.; and Oppen, M. 2020. Interacting particle solutions of fokker-planck equations through gradient-log-density estimation. *Entropy*, 22(8): 802.
- Paszke, A.; Gross, S.; Massa, F.; Lerer, A.; Bradbury, J.; Chanan, G.; Killeen, T.; Lin, Z.; Gimelshein, N.; Antiga, L.; Desmaison, A.; Köpf, A.; Yang, E.; DeVito, Z.; Raison, M.; Tejani, A.; Chilamkurthy, S.; Steiner, B.; Fang, L.; Bai, J.; and Chintala, S. 2019. PyTorch: An Imperative Style, High-Performance Deep Learning Library. *arXiv:1912.01703*.
- Price, I.; Sanchez-Gonzalez, A.; Alet, F.; Andersson, T. R.; El-Kadi, A.; Masters, D.; Ewalds, T.; Stott, J.; Mohamed, S.; Battaglia, P.; Lam, R.; and Willson, M. 2024. GenCast: Diffusion-based ensemble forecasting for medium-range weather. *arXiv:2312.15796*.
- Raissi, M.; Perdikaris, P.; and Karniadakis, G. E. 2019. Physics-informed neural networks: A deep learning framework for solving forward and inverse problems involving nonlinear partial differential equations. *Journal of Computational physics*, 378: 686–707.
- Song, Y.; Shen, L.; Xing, L.; and Ermon, S. 2021. Solving Inverse Problems in Medical Imaging with Score-Based Generative Models. In *NeurIPS 2021 Workshop on Deep Learning and Inverse Problems*.
- Stuart, A. M. 2010. Inverse problems: a Bayesian perspective. *Acta numerica*, 19: 451–559.
- Sun, Z.; Shen, S.; Cao, S.; Liu, H.; Li, C.; Shen, Y.; Gan, C.; Gui, L.-Y.; Wang, Y.-X.; Yang, Y.; et al. 2024. Aligning Large Multimodal Models with Factually Augmented RLHF. In *Annual Meeting of the Association for Computational Linguistics*.
- Utkarsh, U.; Cai, P.; Edelman, A.; Gomez-Bombarelli, R.; and Rackauckas, C. V. 2025. Physics-Constrained Flow Matching: Sampling Generative Models with Hard Constraints. *arXiv:2506.04171*.
- Wang, H.; Han, J.; Fan, W.; Zhang, W.; and Liu, H. 2025. PhyDA: Physics-Guided Diffusion Models for Data Assimilation in Atmospheric Systems. *arXiv preprint arXiv:2505.12882*.

Wen, G.; Li, Z.; Azizzadenesheli, K.; Anandkumar, A.; and Benson, S. M. 2022. U-FNO – An enhanced Fourier neural operator-based deep-learning model for multiphase flow. arXiv:2109.03697.

Xu, R.; Wang, H.; Kementzidis, G.; Si, C.; and Deng, Y. 2025. APOD: Adaptive PDE-Observation Diffusion for Physics-Constrained Sampling. In *ICML 2025 Workshop on Assessing World Models*.

Zhang, H.; Li, Y.; and Huang, J. 2024. DiffusionVel: Multi-Information Integrated Velocity Inversion Using Generative Diffusion Models. arXiv:2410.21776.

Zhang, L.; Rao, A.; and Agrawala, M. 2023. Adding conditional control to text-to-image diffusion models. In *Proceedings of the IEEE/CVF international conference on computer vision*, 3836–3847.

Zhang, Y.; and Zou, D. 2025. Physics-Informed Distillation of Diffusion Models for PDE-Constrained Generation. *arXiv preprint arXiv:2505.22391*.

A Dataset Details

In this section we detail the datasets used throughout our study. Our guiding principle was to select scenarios in which the underlying parameter fields contain sharp discontinuities, thereby inducing rich, non-linear behaviour in the associated state variables and making the inverse problem decidedly non-trivial. Although the Darcy-flow benchmark follows the setup of Li et al. (2021), we regenerate the data so that the sample count, grid resolution, and ground-truth parameters can be controlled precisely. Complete scripts for producing both the Darcy and acoustic datasets will be released to facilitate transparency and reproducibility.

Darcy Flow Dataset. Each sample comprises a permeability field a and its steady-state pressure solution u on the unit square $\Omega = [0, 1]^2$. The PDE

$$-\nabla \cdot (a(\xi) \nabla u(\xi)) = f(\xi),$$

is discretised on a 64×64 grid with a five-point finite-difference stencil and harmonic averaging of a ; the source is fixed to $f \equiv 1$. For the denoising experiments we consider $u|_{\partial\Omega} = 0$, and for misspecified boundary conditions we set $u|_{\partial\Omega}(\xi_1, 1) = \sin(\pi \xi_1)$.

Permeability field. A zero-mean Gaussian random field is generated by a Karhunen–Loève expansion with smoothness exponent $\alpha = 2$ and correlation length $\tau = 3$. To mimic sharply contrasting media, the field is mapped to a binary permeability: $a(\xi) = 12$ if the raw GRF is non-negative and $a(\xi) = 3$ otherwise.

Dataset Size. We compute 20,000 independent (a, u) pairs, each stored at single-precision on the 64×64 grid.

Samples from this dataset are shown in Fig. 5, Fig. 6, and Fig. 7 for the clean, noisy and misspecified setting respectively.

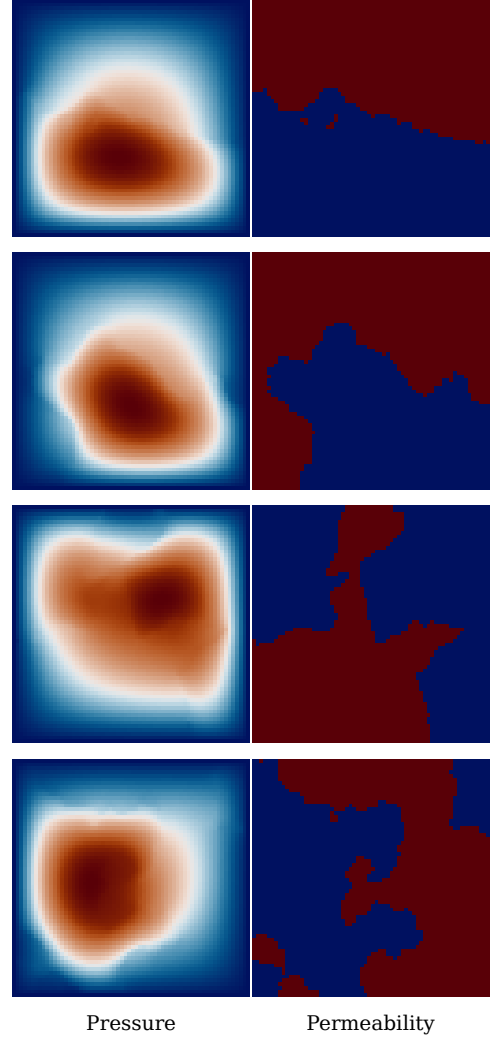


Figure 5: Samples from the (clean) Darcy dataset described in Appendix A.

Acoustic Wave Dataset. We model pressure propagation in a heterogeneous medium governed by

$$\begin{aligned} \partial_t^2 p(t, \xi) - c(\xi)^2 \Delta p(t, \xi) &= 0, & (\xi, t) &\in \Omega \times [0, T] \\ \partial_n p(t, \xi) &= 0, & (\xi, t) &\in \partial\Omega \times [0, T] \\ p(0, \xi) &= h(\xi) \end{aligned}$$

with $\Omega = [0, 1]^2$. The speed of sound $c(\xi)$ is obtained similarly to the permeability in the Darcy data set: a sample from a GRF is thresholded to produce a binary field. Here, the speed of sound takes the values $\{2, 3\}$, and smoothness exponent and correlation length are set to $\alpha = 2$ and $\tau = 1$ respectively.

Initial Condition. The pressure at $t = 0$ is a superposition of four identical isotropic Gaussians centred at $(\frac{i}{3}, \frac{j}{3})$ for

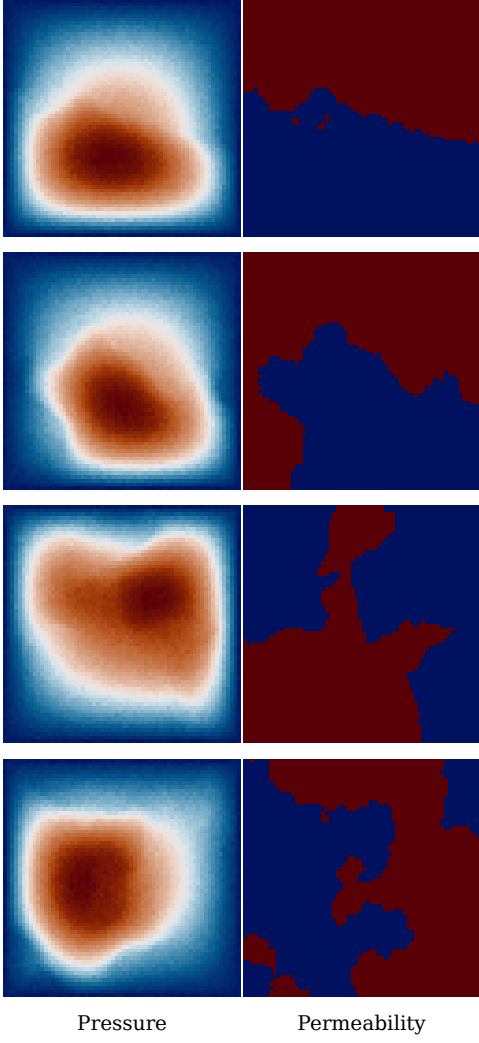


Figure 6: Samples from the noisy Darcy dataset described in Appendix A.

$i, j \in \{1, 2\}$:

$$p(0, \xi) = \sum_{i,j=1}^2 \exp\left(-\frac{\|\xi - (i/3, j/3)\|^2}{2\sigma^2}\right),$$

with common variance $\sigma^2 = 10^{-2}$.

Numerical Solver. Spatial derivatives are discretised on a 64×64 grid using a second-order centred Laplacian with reflective padding. Time integration employs the standard leap-frog scheme with step size $\Delta t = 10^{-3}$. Solutions are recorded every ten five steps, yielding 64 frames in total so that each sample forms a $64 \times 64 \times 64$ space-time tensor with a total time range of $t \in [0, 0.315]$.

Dataset Size. We generate 10 000 independent (p, c) pairs under the above settings, stored in single precision.

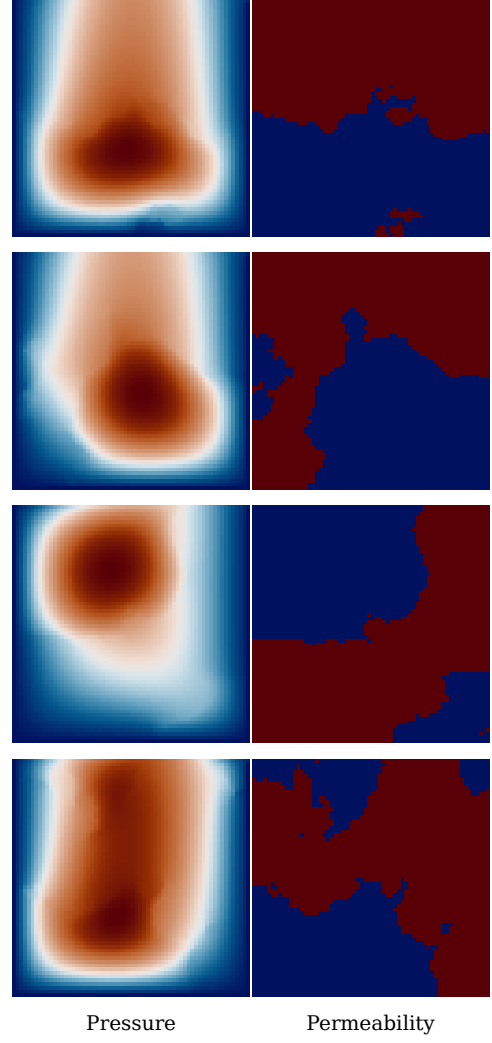


Figure 7: Samples from the Darcy dataset using a sinusoidal boundary condition on the top edge described in Appendix A.

B Pre-Training of Flow Matching Models

We adopt the vanilla Flow-Matching (FM) procedure of Lipman et al. (2023). Based on the optimal-transport reference flow

$$X_t = \beta_t X_1 + \gamma_t X_0$$

with $\beta_t = t$, and $\gamma_t = 1 - t$, we can define conditional vector field as training targets for a parametric model $v_\theta(x_t, t)$. Given an end-point $x_1 \sim p_{\text{data}}$, the conditional vector field is available as

$$v_t(x|x_1) = \frac{1}{1-t}(x_1 - x).$$

This leads to the simplest form of Flow Matching objectives:

$$\mathcal{L}_{\text{FM}}^{\text{OT}} = \mathbb{E} \|v_\theta(X_t, t) - (X_1 - X_0)\|^2$$

where $X_0 \sim \mathcal{N}(0, I)$, $X_1 \sim p_{\text{data}}$ and $t \sim U[0, 1]$.

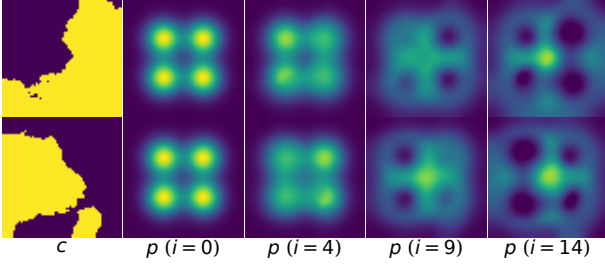


Figure 8: Two samples from the acoustic wave dataset described in Appendix A. The first column shows speed of sound samples from discretized GP which creates different patterns of wave propagation, starting from a superposition of four Gaussians. Evolution per row is shown for discrete time steps indexed by i .

Table 4: U-FNO hyper-parameters used for 2D data.

Spectral modes / dim.	32
Hidden channels	32
Time emb. channels	32
Positional emb. channels	32
FNO layers	0
U-FNO layers	4
Batch size	256
Epochs	500
Initial learning rate	3×10^{-4}
LR decay schedule	$\times 0.5 / 100$ epochs
Parameters	$\approx 17.4\text{M}$
Training time	≈ 6 h

Network Backbone. The mapping v_θ is realised with a U-FNO (Wen et al. 2022). Departing from the original design, we use the U-Net skip-connection structure in all layers. We prepend the physical input with fixed sinusoidal encodings for absolute spatial coordinates and the normalised time stamp so the purely spectral-convolutional backbone receives explicit space-time context without extra learnable parameters. Padding inside the U-FNO (for the spectral convolution layers) is reflective or replicate, matching the PDE’s boundary conditions. Before training, data is standardised to zero mean and unit variance.

Optimisation. Pre-training is performed on a single NVIDIA L40S GPU (48GB GPU memory) with the hyper-parameters listed in Tables 4 for 2D data and 5 for 3D data respectively. The optimiser is Adam with an initial learning rate of 3×10^{-4} (2D) or 5×10^{-4} (3D), halved at the epoch intervals specified in the tables. Training takes roughly six hours for the 2D model (500 epochs, batch size 256) and eight hours for the 3D model (50 epochs, batch size 8).

Figures 9 and 10 present representative pressure-permeability pairs drawn from the Flow-Matching (FM) models trained on the noisy and misspecified Darcy datasets, respectively. Corresponding permeability fields were recovered with the pre-trained inverse predictor φ .

Table 5: U-FNO hyper-parameters used for 3D (space–time) data.

Spectral modes / dim.	16
Hidden channels	32
Time emb. channels	30
Positional emb. channels	30
FNO layers	0
U-FNO layers	2
Batch size	8
Epochs	50
Initial learning rate	5×10^{-4}
LR decay schedule	$\times 0.5 / 10$ epochs
Parameters	$\approx 34.6\text{M}$
Training time	≈ 8 h

Figure 11 shows analogous results for the acoustic-wave dataset. In all three cases the generative models reproduce the salient structures of the data distribution, as evidenced by the fact that φ can invert the generated states back to plausible parameter fields—a task it typically fails on when the synthetic samples deviate from the true manifold. The inverse predictions for the acoustic setting appear blurrier than those for Darcy. We attribute this to an architectural compromise made for computational efficiency, laid out in the next section: φ inherently is designed as a 2D architecture that treats the 64 time frames as input channels, so temporal information is fused already in the lifting layer. A 3D backbone with later fusion stages would likely recover sharper time-independent sound-speed maps, albeit at higher computational cost.

C Method: Implementation Details

In this section, we provide further details into the implementation of our method. This includes neural network architectures, the specific design of test functions for the computation of the weak residuals, numerical heuristics, and finally the full training algorithm for fine-tuning.

All relevant code is implemented using Python 3.12.3, specifically, neural architectures are implemented in PyTorch (Paszke et al. 2019) version 2.7.

Inverse Predictor φ

We parametrise the inverse map φ with a two-layer U-FNO, mirroring the spectral–spatial bias of the forward backbone. All other parameters are identical to the respective U-FNO for the vector field. For the 2D case the network operates on $(H \times W)$ tensors and outputs a permeability field of identical resolution. In the 3D setting we considered a time-independent parameter. Therefore, we collapse the temporal axis into input channels and apply a 2D U-FNO that performs spectral convolutions and U-Net operations solely in the spatial dimensions, yielding a $(H \times W)$ speed-of-sound map at substantially lower computational cost.

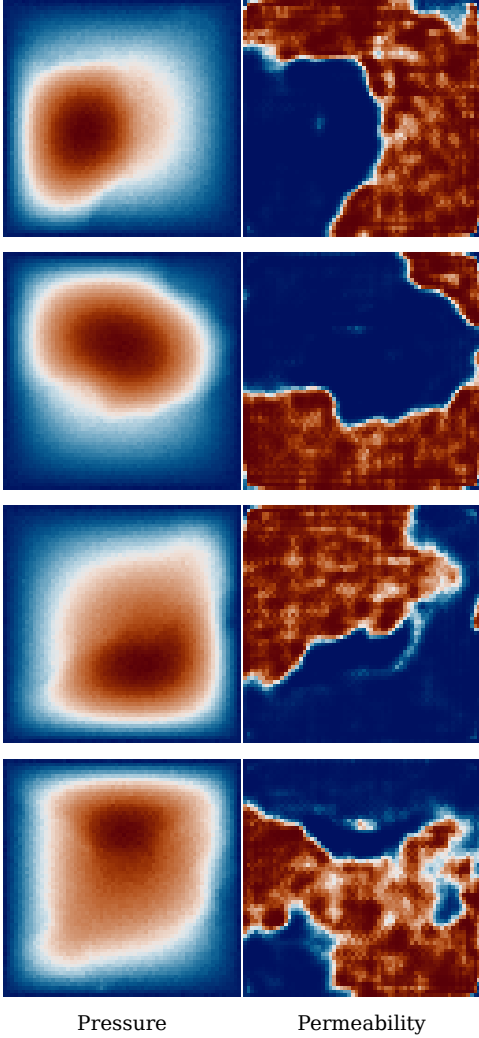


Figure 9: Samples from a pre-trained FM model on the noisy Darcy dataset, including recovered permeabilities from a trained inverse predictor (right column).

Architecture Modifications

Fine-tuning requires extending the original mapping

$$v_{t,x} \leftarrow v(x, t)$$

to a joint vector field

$$(v_{t,x}^{\text{ft}}, v_{t,\alpha}^{\text{ft}}) \leftarrow v^{\text{ft}}(x, \alpha, t).$$

Thus α must be supplied to the network as an additional input (so that $v_{t,x}^{\text{ft}}$ can be *conditioned* on it), and a second output channel $v_{t,\alpha}^{\text{ft}}$ has to be generated.

In practice a lightweight residual modification suffices. We first compute the padded U-FNO output as in the base model. A *correction U-Net* then receives three tensors—the preliminary vector field, the current state x_t^{ft} , and the parameter α_t^{ft} —and produces an additive refinement. After removing the padding, the sum constitutes $v_{t,x}^{\text{ft}}$.

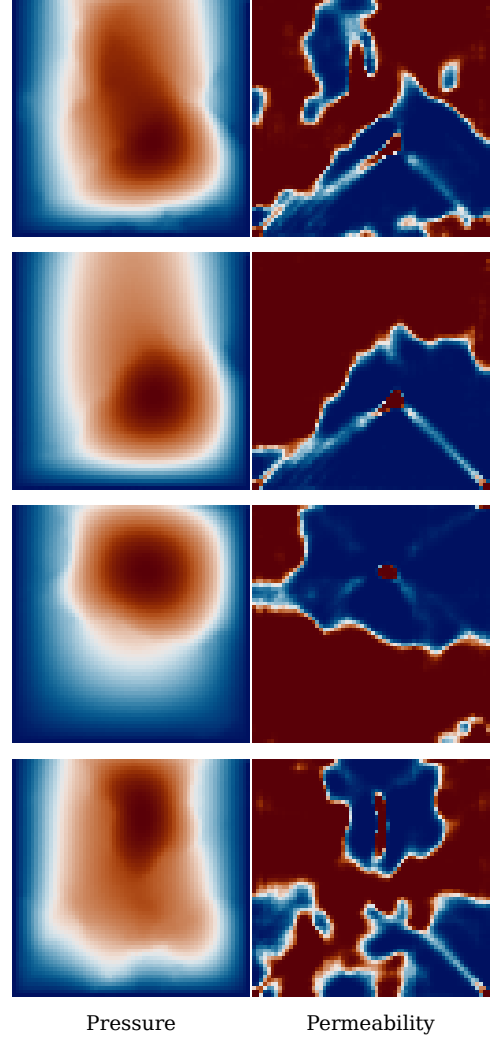


Figure 10: Samples from a pre-trained FM model on the Darcy dataset with misspecified, including recovered permeabilities from a trained inverse predictor (right column).

Learning $v_{t,\alpha}^{\text{ft}}$ from scratch would amount to training an entire denoising process for α during fine-tuning, which is impractical without supervised pre-training. Instead we adopt a residual strategy:

$$v_{t,\alpha}^{\text{ft}} = v_{t,\alpha}^{\text{base}} + \text{U-Net}(v_{t,\alpha}^{\text{base}}, x_t^{\text{ft}}, \alpha_t^{\text{ft}}).$$

Both correctional U-Nets end with a 1×1 convolution, such that pixel-wise corrections can be learned efficiently. Weights and biases of these final layers are initialised to zero so that, at the onset of fine-tuning, the fine-tuned model exactly reproduces the base model and departures are learned gradually.

Weak Residuals and Test Functions

Darcy Flow. Let u solve $-\nabla \cdot (a \nabla u) - f = \mathcal{L}_a u = 0$ on $\Omega \subset \mathbb{R}^d$ with homogeneous Dirichlet data $u|_{\partial\Omega} = 0$.

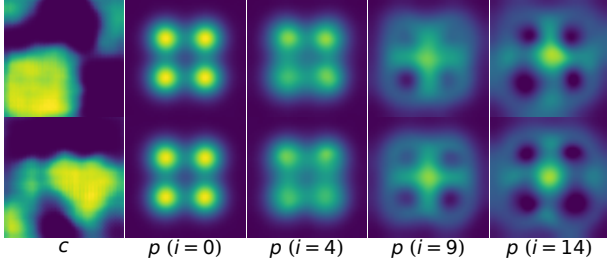


Figure 11: Samples from a pre-trained FM model on the acoustic wave dataset, including recovered speed of sound coefficient fields from a trained inverse predictor. Temporal evolution is displayed for discrete time steps indexed by i .

For any $\psi \in C_0^1(\Omega)$ we compute the L^2 inner product by multiplying with ψ and integrating:

$$\langle \mathcal{L}_a u, \psi \rangle_{L^2(\Omega)} = \int_{\Omega} (-\nabla \cdot (a \nabla u) - f) \psi \, d\xi$$

One application of the divergence theorem yields

$$\begin{aligned} \langle \mathcal{L}_a u, \psi \rangle_{L^2(\Omega)} &= - \int_{\partial\Omega} (a \nabla u \cdot n) \psi \, d\xi \\ &\quad + \int_{\Omega} (a \nabla u \cdot \nabla \psi) - f \psi \, d\xi \\ &= \int_{\Omega} (a \nabla u \cdot \nabla \psi) - f \psi \, d\xi, \end{aligned}$$

where the boundary term vanishes because of $\psi|_{\partial\Omega} = 0$. This expression only contains a first-order derivative of u and can be used to compute in the computation of the weak residual.

Acoustic Wave Equation. Let the pressure field

$$p : \Omega \times [0, T] \rightarrow \mathbb{R}$$

satisfy $\mathcal{L}_c p := \partial_t^2 p - c^2 \Delta p = 0$ with reflective (Neumann) boundary conditions $\partial_n p|_{\partial\Omega} = 0$. For a test function $\psi \in C_0^1(\Omega \times [0, T])$ we form the L^2 -inner product

$$\langle \mathcal{L}_c p, \psi \rangle_{L^2(\Omega \times [0, T])} = \int_0^T \int_{\Omega} (\partial_t^2 p - c^2 \Delta p) \psi \, d\xi \, dt.$$

Integrating the first term once in time and the second term once in space yields

$$\begin{aligned} \langle \mathcal{L}_c p, \psi \rangle_{L^2} &= - \int_0^T \int_{\Omega} \partial_t p \, \partial_t \psi \, d\xi \, dt \\ &\quad + \int_0^T \int_{\Omega} c^2 \nabla p \cdot \nabla \psi \, d\xi \, dt \\ &= \int_0^T \int_{\Omega} (-\partial_t p \, \partial_t \psi + c^2 \nabla p \cdot \nabla \psi) \, d\xi \, dt \end{aligned}$$

where all boundary terms vanish because ψ is compactly supported in both space and time and $\partial_n p = 0$ on $\partial\Omega$. Similar to the Darcy flow, the inner product now contains only first-order derivatives of p .

Wendland-wavelet test family. For estimating the weak residual accurately and to provide a strong learning signal, we need to sample sufficiently many test functions. Evaluating them on the entire computational grid would be prohibitively costly. We therefore consider test functions which are locally supported, such that we can restrict computations to smaller patches. Wendland polynomials are a natural candidate meeting these requirements since they are compactly supported within unit radius and allow for efficient gradient computation. Here, we will describe the test functions in detail.

Each test function is drawn from a radially anisotropic family.

$$\psi_{c,\sigma,b}(x) = \underbrace{(1 - r(x))_+^4}_{\text{Wendland } C^2} \underbrace{(4r(x) + 1)(1 - 64br(x)^4)}_{\text{optional wavelet}},$$

where $r(x) = \sqrt{\sum_j (x_j - c_j)^2 / \sigma_j^2}$. The centre c is uniform in Ω and axis length-scales σ_j are uniform in $[\sigma_{\min} \Delta_j, \sigma_{\max} \Delta_j]$. By multiplying σ_{\min} and σ_{\max} with the grid spacing Δ_j of axis j , we obtain a parametrization that is intuitive to tune since the length-scales of the test functions are given in *pixel* units. $b \sim \text{Ber}(p)$ randomly toggles a high-frequency wavelet factor that provides additional variability within the test functions and proved especially effective on noisy data.

To enforce $\psi_i|_{\partial\Omega} = 0$, we multiply every test function by a *bridge mollifier*

$$m(\xi) = ((\xi - \xi_{\min})(\xi_{\max} - \xi)) / (\xi_{\max} - \xi_{\min})^2,$$

applied per axis. This legitimises the application of integration-by-parts in the derivation of the weak forms.

Note that in many systems the parameter itself scales the weak form. For Darcy flow, for instance, a perturbation that increases ∇u is linearly amplified by the permeability. If left unchecked, a joint optimiser can reduce the loss merely by driving the parameter toward smaller values. To avoid this degeneracy we normalise each test-function residual by the integral of α over the support of that function.

At training time we draw N_{test} $\{\psi^{(i)}\}$ per residual evaluation and define the loss as

$$\mathcal{R}_{\text{weak}}(x, \alpha) = \frac{1}{N_{\text{test}}} \sum_i |\langle \mathcal{L}_\alpha x, \psi^{(i)} \rangle_{L^2}|^2.$$

Heuristics

Similar to the heuristics stated in Domingo-Enrich et al. (2025), to allow for an efficient implementation, we deviate from the theoretical derivations outlined before. We lay them out in this section.

Memoryless Noise. The memoryless noise schedule $\sigma(t) = \sqrt{2\eta_t}$ in our setting of $\beta_t = t$ and $\gamma_t = 1 - t$ can be simplified to

$$\sigma(t) = \sqrt{\frac{2(1-t)}{t}},$$

which causes numerical problems for $t = 0$. Furthermore, it forces the control u to be close to zero for t close to 1. Following the original paper, we instead use

$$\sigma(t) = \sqrt{\frac{2(1-t+h)}{t+h}},$$

where we choose h as the step size of our numerical ODE/SDE solver. This resolves infinite values and allows for faster fine tuning by letting the fine-tuned model deviate further from the base model close to $t = 1$.

Our PDE based fine-tuning residuals are particularly sensitive to noise. Therefore, we must ensure that sampled trajectories are fully denoised. When using memoryless noise, we found that we had to increase the number of steps per sampling trajectory to achieve the same quality of output compared to the ODE-based sampler. For denoising, especially the last steps of sample generation are important. As a trade-off between computational cost and accuracy, we implemented the following strategy: before fine-tuning we decide on a coarse time grid

$$0 = t_0 < \dots < t_{T-1} = 1$$

that will also be used for all test-time rollouts, ensuring a fair comparison with the base model. During fine-tuning we subdivide the last K_{sub} intervals geometrically: the last interval $[t_{T-2}, t_{T-1}]$ is split into K_{sub} equal sub-steps, the previous one into $K_{\text{sub}} - 1$, and so on. Formally, interval $[t_{T-m-1}, t_{T-m}]$ receives $K_{\text{sub}} - m$ internal points for $m = 0, \dots, K_{\text{sub}} - 1$

At inference time we revert to the original T -point grid for both base and fine-tuned models. Thus every quantitative comparison reported in the main paper is based on identical rollout budgets, while the fine-tuned model benefits from the cleaner gradients provided by the adaptive tail refinement during training.

Loss Computation. As in the original paper, we do not compute the Adjoint Matching loss (Equation 3) for all simulated time steps, since the gradient signal for successive time steps is similar. Note that for solving the lean adjoint ODE, we do not need to compute gradients through the FM model, therefore we can compute the lean adjoint states efficiently but save computational resources when computing the Adjoint Matching loss. Again, the last steps in the sampling process are most important for empirical performance. For that reason, we also compute the loss for a fraction of last steps K_{last} . Additionally, we sample K steps from the remaining time steps.

To ensure stable learning, we apply a clipping function to the loss to exclude noisy high-magnitude gradients from training. Empirically, the values provided in Domingo-Enrich et al. (2025) work well in our setting, i.e. we set the loss clipping threshold (LCT) as $\text{LCT}_x = 1.6 \lambda_x^2$ and $\text{LCT}_\alpha = 1.6 \lambda_\alpha^2$ respectively.

Full Training Algorithm

Algorithm 1 details the complete optimisation loop used in all experiments. Starting from the pre-trained base flow v^{base}

we attach two residual heads that (i) condition the state flow $v_{t,x}^{\text{ft}}$ on the latent parameter α and (ii) predict the parameter flow $v_{t,\alpha}^{\text{ft}}$. The inverse predictor φ is first pre-trained on base samples and then frozen, providing surrogate target flows for α . Each epoch rolls both the base and fine-tuned trajectories on an augmented time grid, solves the lean-adjoint equation, and updates only the fine-tune parameters θ through the Adjoint-Matching loss.

Algorithm 1: Adjoint Matching on Joint Evolution

Input: initialise core $v^{\text{ft}} \leftarrow v^{\text{base}}$, add residual-style output heads to get $v_x^{\text{ft}}, v_\alpha^{\text{ft}}$

- 1: **Pretrain** φ based on x_1 samples generated with v_x^{base} by minimizing $\mathcal{R}_{\text{weak}}(x_1, \varphi(x_1))$
 - 2: **Freeze** weights of v_x^{base} and φ , denote trainable parameters as θ
 - 3: **for** number of epochs **do**
 - 4: $x_0 \sim \mathcal{N}(0, I), \quad \alpha_0 \sim \mathcal{N}(0, I)$
 - 5: $\bar{T} \leftarrow \text{GET_AUGMENTED_TIME}(T)$
 - 6: **for** $i \in [\bar{T}]$ **do**
 - 7: $t \leftarrow \bar{T}_i, \quad t^+ \leftarrow \bar{T}_{i+1}, \quad h \leftarrow t^+ - t$
 - 8: $v_{x,t}^{\text{base}} \leftarrow v^{\text{base}}(x_t, t)$
 - 9: $v_{\alpha,t}^{\text{base}} \leftarrow \frac{\hat{\alpha}_1^{\text{ft}} - \alpha_t}{1-t}$
 - 10: $v_{x,t}^{\text{ft}}, v_{\alpha,t}^{\text{ft}} \leftarrow v^{\text{ft}}(x_t, \alpha_t, v_{x,t}^{\text{base}}, t)$
 - 11: $x_{t^+}^{\text{base}} \leftarrow \text{SDE_STEP}(x_t^{\text{base}}, v_{x,t}^{\text{base}}, \sigma(t), h)$
 - 12: $x_{t^+}^{\text{ft}} \leftarrow \text{SDE_STEP}(x_t^{\text{ft}}, v_{x,t}^{\text{ft}}, \sigma(t), h)$
 - 13: $\alpha_{t^+}^{\text{ft}} \leftarrow \text{SDE_STEP}(\alpha_t^{\text{ft}}, v_{\alpha,t}^{\text{ft}}, \sigma(t), h)$
 - 14: **end for**
 - 15: $\tilde{a} \leftarrow \text{SOLVE_LEAN_ADJOINT}(x^{\text{base}}, x^{\text{ft}}, \alpha^{\text{ft}})$
 - 16: $\theta \leftarrow \text{GRADIENT_DESCENT}(\theta, \mathcal{L}(\tilde{u}; \tilde{X}, \tilde{a}))$
 - 17: **end for**
 - 18: **return** v^{ft}, φ
-

D Details: Experimental Results

Hyperparameters for Experimental Results

Before starting fine-tuning, we train the inverse predictor φ . In 2D, we generate 1024 samples x_1 from the base model, in 3D we use 512. On these samples, the inverse predictor is trained for 100 epochs to minimize the weak residual $\mathcal{R}_{\text{weak}}(x_1, \varphi(x_1))$. As the optimizer, we use Adam with a learning rate of 1×10^{-4} and a batch size of 8.

For fine-tuning, all runs use Adam with a fixed learning rate 2×10^{-5} and are trained on a single NVIDIA L40S GPU (48 GB). The settings that differ across tasks are summarised below.

Darcy Experiments

	Denoising	Misspec.
Time horizon T	100	100
Tail fraction K_{last}	0.20	0.20
Evaluation steps K	20	20
Tail refinement K_{sub}	5	5
# test functions	4096 (one per grid point)	
$[\sigma_{\min}, \sigma_{\max}]$	$[3, 10]$	$[1, 20]$
Epochs	200	1000
Batch size	6	6
Runtime	≈ 30 min	≈ 2.5 h

In 2D, it is computationally feasible to sample one test function centered at each grid point. To still have stochasticity in location of test functions but ensure good spatial coverage, we sample small offsets that we add to each grid point. The fine-tuning network has ≈ 19 M parameters and the inverse predictor ≈ 9 M.

Acoustic Experiment

Sampling steps T	40
Tail fraction K_{last}	0.25
Evaluation steps K	10
Tail refinement K_{sub}	3
# test functions	1000
Super-resolution factor	4
σ range	$[1, 20]$
Epochs	400
Effective batch ($4 \times$ grad. accum.)	8
Runtime	≈ 12 h

Here the fine-tuning network has ≈ 39 M parameters, the inverse predictor remains at ≈ 9 M. In 3D, especially when upsampling by a factor of 4, test function evaluation and network evaluations are significantly more expensive than the respective operations in 2D.

Point-wise Distribution Metrics

Following Kerrigan, Migliorini, and Smyth (2023), we compare data and model by averaging statistics which describe similarity at every grid point. Denote by $\mu_{\text{data}}(\xi)$, $\sigma_{\text{data}}(\xi)$ the empirical mean and standard deviation at location $\xi \in \Omega$ and by $\mu_{\text{gen}}(\xi)$, $\sigma_{\text{gen}}(\xi)$ the corresponding quantities estimated from generated samples. All scores are normalised by the average data variance

$$S_{\text{data}} = \frac{1}{|\Omega|} \sum_{\xi} \sigma_{\text{data}}^2(\xi).$$

Mean mismatch

$$\text{MMSE}_{\text{rel}} = \frac{1}{S_{\text{data}}|\Omega|} \sum_{\xi} (\mu_{\text{gen}} - \mu_{\text{data}})^2.$$

Spread mismatch

$$\text{SMSE}_{\text{rel}} = \frac{1}{S_{\text{data}}|\Omega|} \sum_{\xi} (\sigma_{\text{gen}} - \sigma_{\text{data}})^2.$$

Ensemble diversity

$$\text{Diversity}_{\text{rel}} = \frac{1}{S_{\text{data}}|\Omega|} \sum_{\xi} \sigma_{\text{gen}}^2(\xi).$$

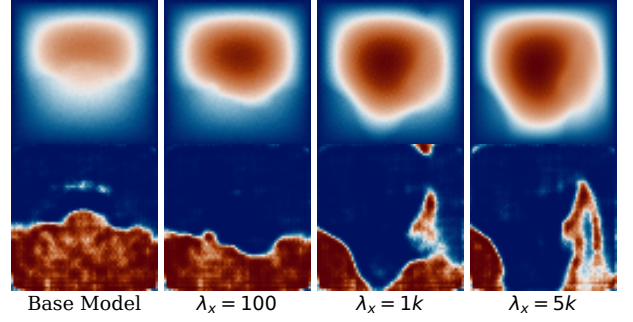


Figure 12: Fine-tuned models for pre-trained model on noisy data without regularization, $\lambda_f = 0$ for different fine-tuning strengths λ_x . The top row shows the pressure distribution induced by the permeability in the second row.

For the ensemble diversity, a score of 1 indicates parity with the data; values < 1 denote less variability, whereas values > 1 reveal increased point-wise variance in generated samples. All three metrics are dimensionless and therefore comparable across datasets and resolutions.

E Additional Results

Denoising

Details on Denoising with $\lambda_f = 0$. To further illustrate the effectiveness of our proposed regularization, we here demonstrate that similar results cannot be obtained by simply reducing the fine-tuning strength λ_x . Figure 12 shows fine-tuning results for $\lambda_f = 0$ and $\lambda_x \in \{100, 1000, 5000\}$. For small λ_x , fine-tuning retains some similarity to the sample of the base model, but does not lead to fully denoised samples. On the other hand, fully denoised samples for high values of λ_x have diverged far from the samples of the base model, and, as Table 2 indicates, show signs of mode collapse.

Regularization Strength λ_f . For a fixed $\lambda_x = 15k$, we here compare results from fine-tuning with different regularization strengths $\lambda_f \in \{0.001, 0.01, 0.1\}$. Here, all models are able to produce visually denoised samples, see Fig. 13. However, for lower values of regularization we again see a higher deviation from the base sample, both for the obtained pressure and permeability, similar to higher λ_x in the previous example.

Residual Heatmaps. We can visually represent the weak residuals as heatmaps by computing the inner product $\langle \mathcal{L}_a u, \psi^{(i)} \rangle_{L^2(\Omega)}$ for each spatial location with a test function centered at the respective coordinates. In this case, to ensure comparability, length-scales are not sampled but fixed. Figure 14 shows such heatmaps the fine-tuned model trained on the denoising task. Note that the model was fine-tuned with $\sigma \in [3, 10]$, but the residual was also decreased for larger length-scales.

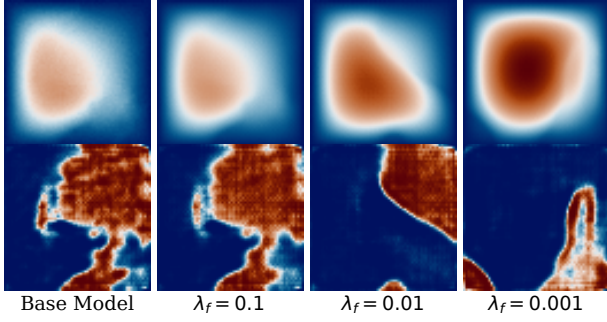


Figure 13: Fine-tuned models for pre-trained model on noisy data with different levels of regularization λ_f for the same λ_x . The top row shows the pressure distribution induced by the permeability in the second row.

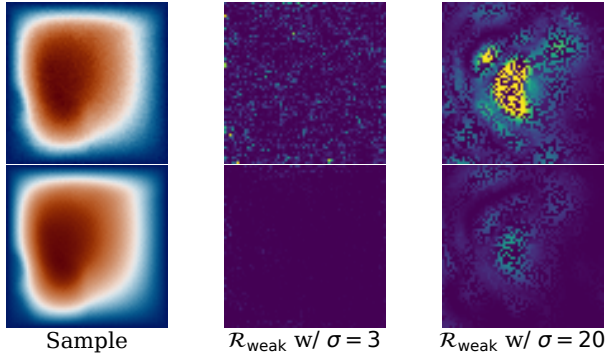


Figure 14: Heatmaps of residual for fine-tuned model on de-noising task, showing residuals computed with two distinct length-scales for the test functions.

Guidance

We provide more samples obtained from guided samples based on sparse observations on the parameter. Here, we show samples for $m \in \{10, 100, 1000\}$ in, Fig 19, Fig 20, and Fig 21 respectively. As expected, the variability of generated samples reduces drastically with an increased number of observations. Sparse observations are sampled from ground-truth training data. As indicated in Table 2, the base Flow Matching models show a reduced variability in the recovered parameter - an issue which might be resolved by for example using more training data or stronger base models. Therefore, we cannot expect that the model can be guided perfectly towards *all* parameter fields in the training data. However, results from guided generation follow the sparse observations quite accurately.

Acoustics

Figure 15 shows a sample from the base FM model (with speed of sound recovered from pre-trained inverse predictor) and the fine-tuned model on four times upsampled data.

Since the scalar boundary loss reported in the main paper aggregates violations of the reflective condition over space

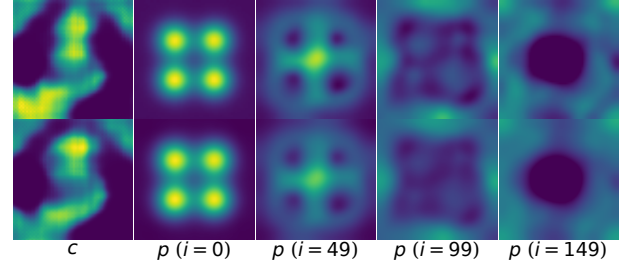


Figure 15: Top row: generated sample from base FM model trained on acoustic wave data of resolution $64 \times 64 \times 64$. Second row: sample from fine-tuned model on upsampled data ($256 \times 256 \times 256$) for same initial noise. Time indices for sample from base model are adapted to match fine-tuned ones.

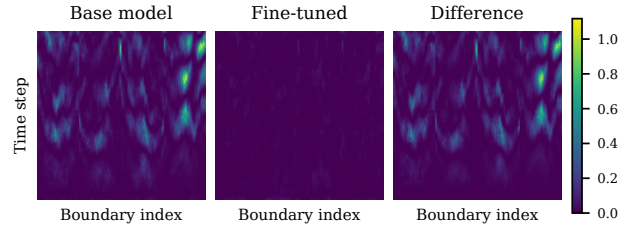


Figure 16: Squared magnitude of the normal pressure gradient along the reflective boundary in the acoustic-wave experiment.

and time, localised spikes can be obscured by averaging. To reveal the full spatio-temporal behaviour we visualise, in Fig. 16, the evolution of the squared normal-gradient magnitude $|\nabla_n p|^2$.

For a generated trajectory we concatenate the four spatial edges of the upsampled output into a single “boundary index” axis of length $4(H-2) = 1016$ and stack the resulting vectors over the 256 time steps, producing a 256×1016 matrix per model. We display the residuals for the base and fine-tuned model and the difference (base - fine-tuned). It can be seen that the fine-tuned model effectively suppresses boundary spikes uniformly across time.

Boundary Misspecification

Without regularization, fine-tuning a FM model trained on the misspecified data is extremely prone to collapse. Even for moderately successful fine-tuning, where the distribution has not learned yet to follow the imposed boundary condition, we can see a strong shift in the recovered parameter. Without regularization, we did not manage to fine a good set of hyperparameters to produce good results.

Fine-tuning in the misspecified-boundary setting is particularly demanding: both the generative backbone and the inverse predictor have been pre-trained on data that violate the target boundary condition, so the new task lies well outside their training distribution. Surprisingly, the ECI method

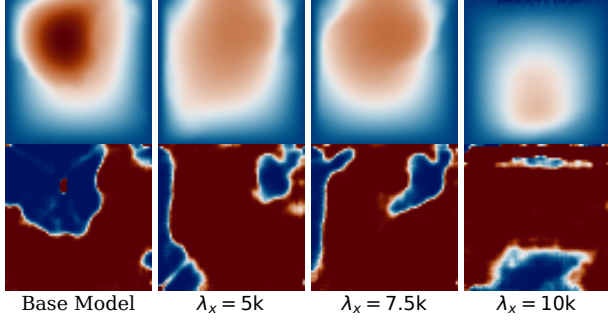


Figure 17: Fine-tuning results with $\lambda_f = 0$ for different strengths λ_x

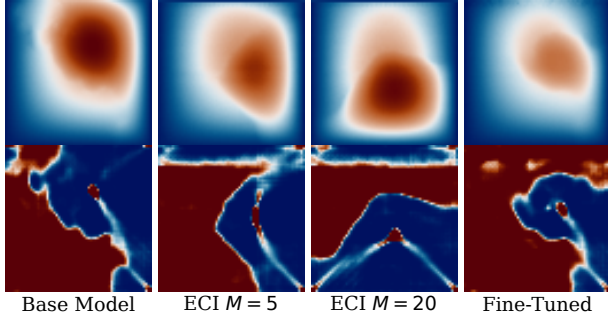


Figure 18: Comparison of ECI sampling with post-training fine-tuning to enforce 0 boundary conditions along the top edge. Parameter estimates for ECI samples are inferred from the pre-trained predictor φ .

(Cheng et al. 2024) yields pressure fields that remain qualitatively consistent with the governing physics. This suggests that the base FM model already internalises much of the underlying structure. For ECI, we tested the number of mixing steps $M \in \{0, \dots, 20\}$ and report the (visually) best results in Fig. 18. However, the ECI samples deviate significantly from the base sample, whereas our fine-tuning procedure preserves detail through the parameter field. Although the comparison is not entirely fair—ECI is gradient-free and oblivious to PDE residuals—it highlights a broader limitation of inference-time adaptation: without physics-aware guidance such methods may satisfy the boundary condition only at the cost of drifting away from the learned data distribution. A promising hybrid approach could be to apply such inference-time projection methods to our fine-tuned model.

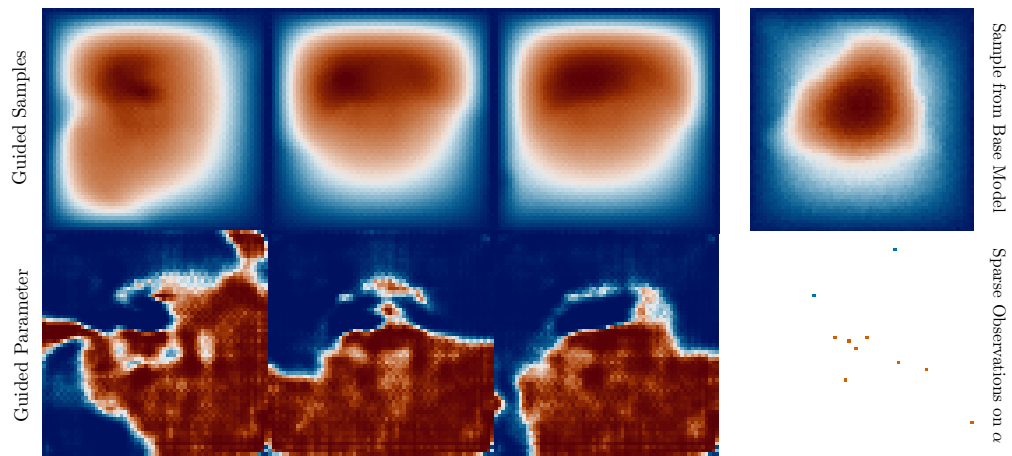


Figure 19: Additional results on guided sampling. Setup is identical to Fig. 3 except of number of sparse observation ($m = 10$).

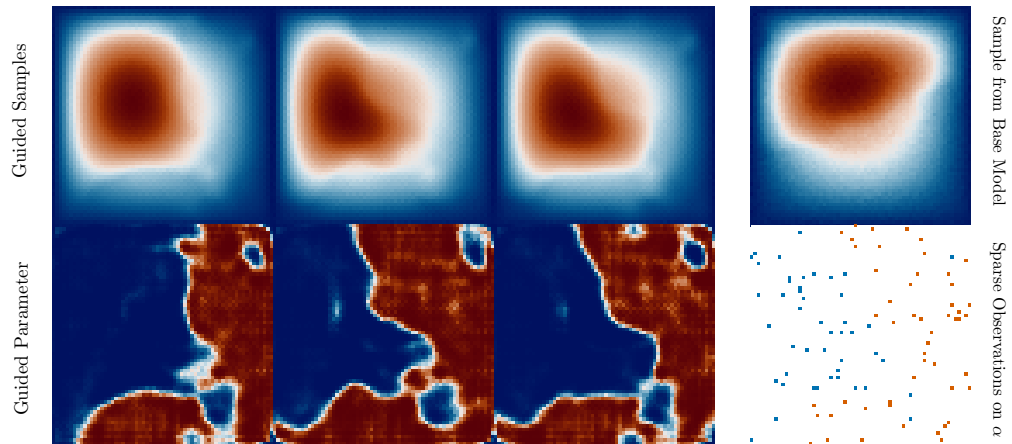


Figure 20: Additional results on guided sampling. Setup is identical to Fig. 3 except of number of sparse observation ($m = 100$).

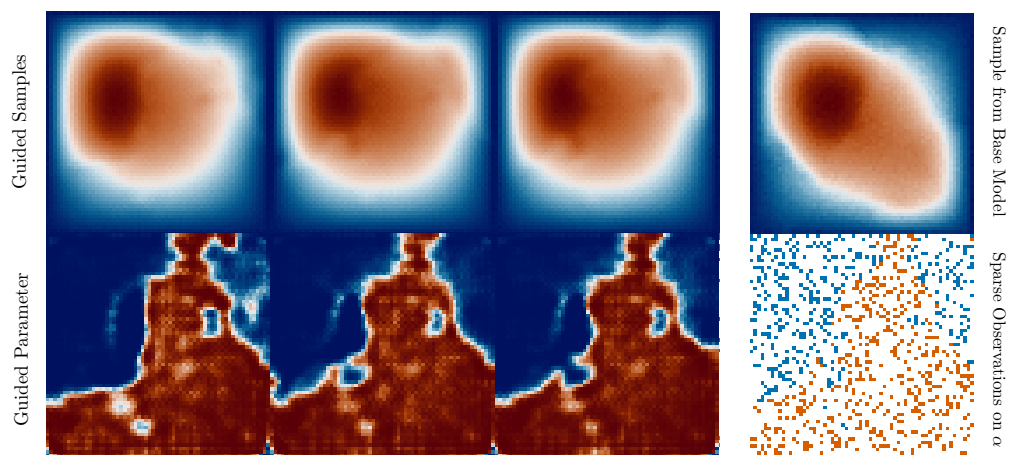


Figure 21: Additional results on guided sampling. Setup is identical to Fig. 3 except of number of sparse observation ($m = 1000$).